Energy Storage Materials 17 (2019) 178–185

Contents lists available at ScienceDirect

Energy Storage Materials

journal homepage: www.elsevier.com/locate/ensm

Graphene-tailored molecular bonds for advanced hydrogen and lithium storage performance

Yuqin Huang[a,b], Guanglin Xia[b,*], Jian Zhang[c], Zaiping Guo[b], Xuebin Yu[a,d,**]

[a] Department of Materials Science, Fudan University, Shanghai 200433, China
[b] Institute for Superconducting and Electronic Materials, University of Wollongong, North Wollongong, NSW 2522, Australia
[c] Hunan Provincial Key Laboratory of Safety Design and Reliability Technology for Engineering Vehicles, Changsha University of Science and Technology, Changsha 410114, China
[d] Shanghai Innovation Institute for Materials, Shanghai 200444, China

ARTICLE INFO

Keywords:
Alanates
Hydrogen storage
Graphene
Thermodynamics
Complex hydrides

ABSTRACT

The practical application of sodium alanate ($NaAlH_4$) as a hydrogen and lithium storage material has attracted intensive attention. The high energy barrier for breaking the Al-H bonds of $NaAlH_4$, however, remains a key challenge. Here, we report that graphene could act as an effective platform to tailor the metal-hydrogen bonds of $NaAlH_4$ through their favorable molecular interaction. Theoretical and experimental results confirm that graphene is capable of weakening the Al-H bonds of $NaAlH_4$, thus facilitating the breaking and recombination of Al-H bonds towards advanced hydrogen and lithium storage performance. In addition, owing to this favorable interaction, a robust nanostructure composed of homogeneous $NaAlH_4$ nanoparticles with an average size of ~12 nm encapsulated in graphene nanosheets has been developed via a facile solvent evaporation induced deposition method with a tunable loading and distribution. The synergistic effects of the favorable molecular interaction between graphene and $NaAlH_4$ and the noticeable decrease in particle size significantly boost the hydrogen and lithium storage performances of $NaAlH_4$. This method provides new avenues to tailoring the molecular bonds of metal hydrides for a new range of applications in various fields.

1. Introduction

The requirements of clean and renewable energy systems, along with the eagerness from a variety of industries, including large-scale alternative energy, clean transport, and portable electronics, have pushed forward the development of advanced energy storage technologies [1]. Due to their superior energy density, and clean and efficient energy storage mechanism, two promising strategies, *i.e.*, chemical storage of hydrogen in metals or other solid compounds and electrical energy storage in lithium-ion batteries (LIBs) [2–9], have attracted enormous attention.

Sodium alanate ($NaAlH_4$) has been considered as a highly promising hydrogen storage candidate, owing to its high gravimetric (7.5 wt%) and volumetric capacity (94 g H_2 L^{-1}) according to the reversible hydrogen storage reactions as shown below [10,11]:

$$NaAlH_4 \leftrightarrow 1/3Na_3AlH_6 + 2/3Al + H_2\ (3.7\ wt\%,\ \Delta H = 37\ kJ\ mol^{-1}\ H_2) \quad (1)$$

$$Na_3AlH_6 \leftrightarrow 3NaH + Al + 3/2H_2\ (1.9\ wt\%,\ \Delta H = 47\ kJ\ mol{-}^{1}\ H_2) \quad (2)$$

where ΔH is the change in enthalpy.

Theoretical calculations demonstrate that the dehydrogenation enthalpies in these two steps are 37 and 47 kJ mol^{-1} H_2, respectively, corresponding to a dehydrogenation temperature of ~30 and 100 °C, respectively, under the equilibrium pressure of 0.1 MPa, which could satisfy the practical requirements for proton exchange membrane fuel cells (PEMFCs) [12]. Unfortunately, due to its high kinetic barriers induced by its sluggish mass transport, an operating temperature of over 200 °C is required for the dehydrogenation of $NaAlH_4$ [13]. Furthermore, the poor reversibility and slow dehydrogenation kinetics are also important obstacles for the practical application of $NaAlH_4$ as a hydrogen storage material, which is mainly attributable to the grain growth and particle agglomeration upon heating [14,15].

On the other hand, $NaAlH_4$ was recently demonstrated to be a great potential candidate as a new high-energy, low-cost, and sustainable negative electrode for LIBs due to its high theoretical gravimetric capacity of 1985 mA h g^{-1} and moderately low working voltage [16]. Two different lithiation pathways were reported through the following reactions:

* Corresponding author.
** Corresponding author at: Shanghai Innovation Institute for Materials, Shanghai 200444, China.
E-mail addresses: guanglin@uow.edu.au (G. Xia), yuxuebin@fudan.edu.cn (X. Yu).

https://doi.org/10.1016/j.ensm.2018.07.020
Received 21 May 2018; Received in revised form 23 July 2018; Accepted 23 July 2018
Available online 24 July 2018

$$NaAlH_4 + 3/2Li \leftrightarrow 1/2LiNa_2AlH_6 + 1/2Al + LiH \quad (3)$$

$$LiNa_2AlH_6 + 3/2Li \leftrightarrow 2Na + Al + 6LiH \quad (4)$$

Or:

$$NaAlH_4 + 2Li \leftrightarrow 1/3Na_3AlH_6 + 2/3Al + 2LiH \quad (5)$$

$$Na_3AlH_6 + 6Li \leftrightarrow 3Na + Al + 6LiH \quad (6)$$

The complicated electrochemical conversions involved in the lithiation and delithiation processes mean that the $NaAlH_4$ suffers from poor reactivity and reversibility due to its insulating nature and the presence of phase separation, significant volume changes, and the sodium stripping reaction [17–20].

To resolve these issues, various strategies have been proposed to improve the hydrogen and lithium storage performances of $NaAlH_4$, including doping with catalysts [10,21,22] and/or nanostructuring [15,18,20,23,24]. Despite these numerous research efforts, the performance of $NaAlH_4$ still falls far short of the requirements for practical applications. The presence of strong ionic (Na^+ and $[AlH_4]^-$) and covalent interactions (Al–H bonds) in $NaAlH_4$ lead to high energy and kinetics barriers for breaking metal-hydrogen bonds [25]. Therefore, it has been acknowledged that, based on the reaction mechanisms for hydrogen and lithium storage, the strength of the metal-hydrogen bonds, *i.e.*, Al–H bonds in $NaAlH_4$, plays an important role in determining the thermodynamics and kinetics for dehydrogenation (lithiation) and hydrogenation (de-lithiation), which has been widely demonstrated by numerous experimental and theoretical studies [26,27]. It remains a key challenge, however, to controllably tailor the strength of Al–H bonds of alanates towards advanced hydrogen (lithium) storage performance in a way that is not only facile, but also effective.

In the present work, we demonstrate that graphene could act as an effective platform to control and tune the metal-hydrogen bonds of $NaAlH_4$ nanoparticles (NPs) through the favorable molecular interaction between them. Both theoretical calculations and experimental results validate that, owing to the intimate physical contact and the favorable molecular interaction between $NaAlH_4$ and graphene, graphene could effectively weaken the ability of Na to donate charge to the AlH_4 moiety and hence, reduce the strength of the Al–H bond, which could decrease the energy barrier for either H_2 desorption and absorption, or the insertion and extraction of Li ions. Taking advantage of this favorable interaction between $NaAlH_4$ and graphene, a robust nanostructure composed of homogeneous $NaAlH_4$ NPs with an average size of ~ 12 nm encapsulated in graphene nanosheets was fabricated via a facile solvent evaporation induced deposition (SEID) method with tunable loading and distribution (Fig. 1). This unique nanostructure contributes for effective hydrogen and lithium storage in $NaAlH_4$. First, graphene could act not only as a functional support for anchoring well-dispersed $NaAlH_4$ NPs, but also to effectively prevent their aggregation and growth, thus leading to stable cycling performance for hydrogen and lithium storage. Moreover, the fast thermal and electronic conductivity of graphene greatly improves the transfer rate of heat and electrons, leading to fast kinetics for hydrogen and lithium storage [28–30]. Moreover, the homogenous distribution of $NaAlH_4$ on graphene could provide a large surface area and large void space on the surface, which enhance the accessibility of hydrogen and electrolyte, and shorten the diffusion pathways for hydrogen and lithium ions. Owing to these advantages, the nanostructured hybrids of $NaAlH_4$-graphene could show significantly enhanced hydrogen and lithium storage performance.

2. Results and discussion

The $NaAlH_4$@graphene composite (denoted as SAH@G) was fabricated by a facile SEID method via infiltrating $NaAlH_4$ solution (in tetrahydrofuran, THF) into porous graphene nanosheets (GNs). Under the most stable adsorption configuration, density functional theory calculation results verify that the binding energy between $NaAlH_4$ and graphene approaches 0.477 eV (Fig. S1, Supporting Information), which favors the homogeneous distribution of $NaAlH_4$ on the graphene. Mulliken charge analysis demonstrated that, when $NaAlH_4$ clusters interact with graphene, a significant charge is transferred from $(NaAlH_4)_n$ to graphene, which could be verified by the clear overlap between various $NaAlH_4$ clusters and graphene for all the $NaAlH_4$-graphene systems (Fig. 1**b, c** and Fig. S2). It underscores the strong electronic interaction between graphene and $NaAlH_4$. In addition, the energies required to form larger clusters in the presence of graphene are much smaller than that without graphene (Fig. S3), which confirms that $(NaAlH_4)_n$ tends to be uniformly adsorbed on the graphene rather than forming larger clusters. To be specific, graphene could act as an electron acceptor and withdraw electrons from $NaAlH_4$ clusters, and hence, Na^+ ions are pulled toward the graphene planes in the $NaAlH_4$-graphene hybrid. This results in a large charge transfer of 0.06e from the $NaAlH_4$ clusters to graphene, which could effectively reduce the electron donation of Na to the AlH_4 moiety and thus weaken the Al–H bonds of the AlH_4 moiety.

In order to unravel the morphologies of the as-prepared nanostructured composite, field-emission scanning electron microscopy (FE-SEM) was conducted. As shown in Fig. S4a, pure GNs exhibit large-sized lamellar structures with clean surfaces. After the deposition of $NaAlH_4$ on graphene via the SEID method, nanoparticles distributed on the GNs with an average particle size of ~ 10.2 nm could be clearly observed when loaded with 10 wt% $NaAlH_4$ (sample denoted as SAH@G-10) (Fig. S5). More importantly, the homogenous distribution of $NaAlH_4$ NPs is well preserved when the loading rate of $NaAlH_4$ is increased from 10 wt% to 30 and 50 wt%, and only slight growth of particle size of the thus-formed $NaAlH_4$ NPs is observed along with the increased density (Figs. S6 and S7). In particular, when the proportion of $NaAlH_4$ reaches 50 wt% (sample denoted as SAH@G-50), there is still obvious interparticle space between individual $NaAlH_4$ NPs (Fig. 2**a**, **b**), and the average particle size of the as-synthesized $NaAlH_4$ NPs is only 12.4 nm. (Fig. S7). The significant decrease in the particle size could effectively shorten the diffusion pathways for hydrogen and/or lithium ions, which improves the hydrogen and/or lithium storage performance. In strong contrast, without the support and direction provided by graphene, $NaAlH_4$ particles synthesized via the SEID method show a bulk shape with serious aggregation (Fig. S4b). This highlights the important role of the molecular interaction between $NaAlH_4$ and graphene in tuning the formation and distribution of $NaAlH_4$ on the graphene, which provides an enormous number of nucleation and anchoring sites for $NaAlH_4$ NPs and prevents the aggregation of $NaAlH_4$.

Transmission electron microscopy (TEM) image of SAH@G-50 provides additional evidence of the homogeneous distribution of $NaAlH_4$ NPs on GNs (Fig. 2**c**). The scanning TEM (STEM) images (Fig. 2**d-f**) further demonstrate that high-density $NaAlH_4$ NPs are homogenously scattered throughout the surface and interleaved layers of GNs with space in between. This feature is beneficial for accommodating the volume variation and alleviating particle aggregation during cyling dehydrogenation (lithiation) and hydrogenation (de-lithiation). No isolated $NaAlH_4$ NPs were observed in the hybrid, even after ultrasonic treatment for 20 min to disperse the sample for TEM and STEM tests, indicating the strong molecular interactions between $NaAlH_4$ and GNs, which contributes to the uniform formation of $NaAlH_4$ NPs on GNs. The intimate contact between $NaAlH_4$ NPs and GNs with excellent thermal and electron conductivity could significantly improve the transfer of heat and electrons in the hybrid. Additionally, the corresponding energy dispersive X-ray spectroscopy (EDX) mapping (Fig. 2**g-k**) of Na, Al, and C elements in the SAH@G-50 sample indicates that the maps of all three elements apparently match very well with the structure of the as-prepared SAH@G-50,

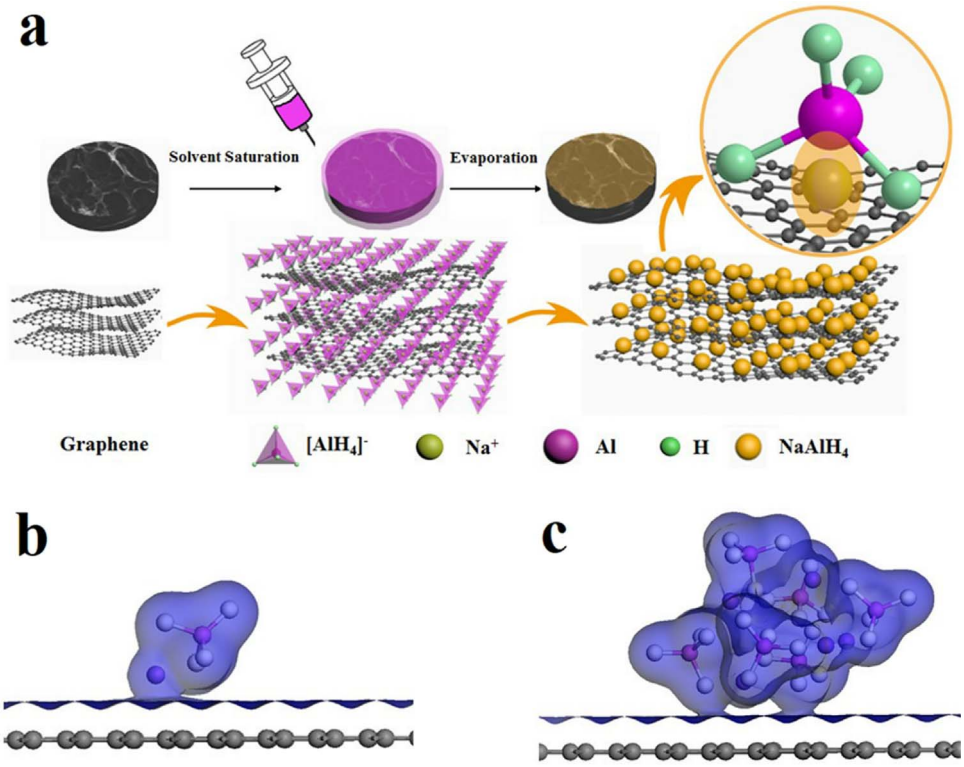

Fig. 1. (a) Schematic illustration of the synthesis of SAH@G-50. Isosurface of electron density of the $NaAlH_4$ on graphene (b) and $(NaAlH_4)_6$ on graphene (c).

which validates the argument that the $NaAlH_4$ NPs are evenly distributed on the GNs. Therefore, it is clearly established that SAH@G-50 shows a compact three-dimensional (3D) stacking nanostructure, in which $NaAlH_4$ NPs are uniformly anchored on the GNs.

The formation of $NaAlH_4$ in SAH@G-50 was confirmed by powder X-ray diffraction (PXRD), and the sample exhibits clear diffraction peaks readily indexed to a pure tetragonal phase of $NaAlH_4$ (Fig. 3**a**). Fourier transform infrared spectroscopy (FTIR) was subsequently adopted to characterize the presence of $NaAlH_4$ on the graphene in SAH@G-50. As shown in Fig. 3**b**, the peaks of the bulk $NaAlH_4$ sample at 1676 cm^{-1} and 736 cm^{-1} correspond to the stretching mode ν_3 of the Al–H vibration and the bending mode ν_4 in the AlH_4 group, respectively. It is interesting to note that, after the homogeneous encapsulation of $NaAlH_4$ in porous GNs, both characteristic peaks of the SAH@G-50 sample obviously shift to lower wavenumbers compared with those of pure $NaAlH_4$, which indicates the weakening of Al–H bond strength in the thus-formed $NaAlH_4$ phase when interacting with graphene. This coincides well with the theoretical calculation results and directly demonstrates the favorable molecular interactions between graphene and $NaAlH_4$. In order to quantitatively verify the weakening of Al-H bonds due to the intimate interaction of $NaAlH_4$ with graphene, the energies required for removing hydrogen from $NaAlH_4$ were calculated based on DFT calculations. It is revealed that the removal energy of hydrogen from $NaAlH_4$ interacting with graphene is only ~ 0.31 eV (Fig. 3**c**), while this value approaches around 1.34 eV without the presence of graphene (Fig. 3**d**). This result directly confirms that graphene could effectively decrease the energy required for breaking and recombination of the Al-H bonds and thereby facilitate the hydrogen and/or lithium storage performance of $NaAlH_4$.

The hydrogen storage performance of the as-prepared SAH@G-50 was first evaluated through thermogravimetric analysis in conjunction with mass spectrometry (TGA-MS) in a comparison with bulk $NaAlH_4$ and the ball-milled $NaAlH_4$/G composite (Fig. 4 and S8). As illustrated in Fig. 4**a**, the H_2 desorption from bulk $NaAlH_4$ starts at about 180 °C, with two main dehydrogenation peaks at temperatures of 257 °C and 279 °C, which could be ascribed to the decomposition of $NaAlH_4$ and Na_3AlH_6, respectively [31]. The first two steps of H_2 desorption that hold great potential for practical application are completed at around 300 °C with a total H_2 capacity of 5.6 wt% (Fig. 4**b**), which is consistent with the theoretical capacity. It should be noted that all the hydrogen capacity in this work is calculated on the mass of $NaAlH_4$. After ball-milling with graphene, the onset dehydrogenation temperature of $NaAlH_4$ was lowered to 150 °C, and the two peak temperatures were reduced to 203 °C and 213 °C, respectively, which are 50 °C and 60 °C lower than for the bulk $NaAlH_4$, respectively. These results demonstrate that graphene could play a catalytic role in the dehydrogenation process of $NaAlH_4$, owing to the somewhat weak interaction between $NaAlH_4$ and graphene in the milled composite. By comparison, taking advantages of the uniform distribution of $NaAlH_4$ on graphene with intimate contact and the significant reduction of particle size down to ~ 12.4 nm, SAH@G-50 exhibits an onset temperature of 100 °C, which is 80 °C and 50 °C lower than for the bulk counterpart and the ball-milled composite, respectively. In addition, a hydrogen capacity of ~ 5.6 wt% could be achieved at a temperature of less than 200 °C, indicating complete dehydrogenation below 200 °C. More interestingly, the two-step dehydrogenation process of $NaAlH_4$ merges into a single hydrogen release peak at a temperature of 153 °C in SAH@G-50. This could be ascribed to the significant reduction in the particle size of $NaAlH_4$ with the homogeneous distribution on GNs, which induces Jahn-Teller distortion in small clusters, so that the decomposition of $NaAlH_4$ occurs in a single step [12,32]. These results verify that the synergetic role of the weakening of Al-H bonds and the reduction of particle size significantly could enhance the hydrogen storage properties of $NaAlH_4$.

Isothermal volumetric desorption measurements at various temperatures were subsequently conducted to investigate the synergetic effects of the weakening of Al-H bonds and the reduction of particle size towards improving hydrogen storage kinetics of $NaAlH_4$ (Fig. 4**c**). It could be clearly observed that, at a temperature of 160 °C, only a negligible amount of hydrogen could be released from bulk $NaAlH_4$ over a period of 100 min, and the ball-milled composite of $NaAlH_4$ and graphene desorbed only 2.5 wt% hydrogen under the same conditions due to the catalytic role of graphene. In strong contrast, SAH@G-50

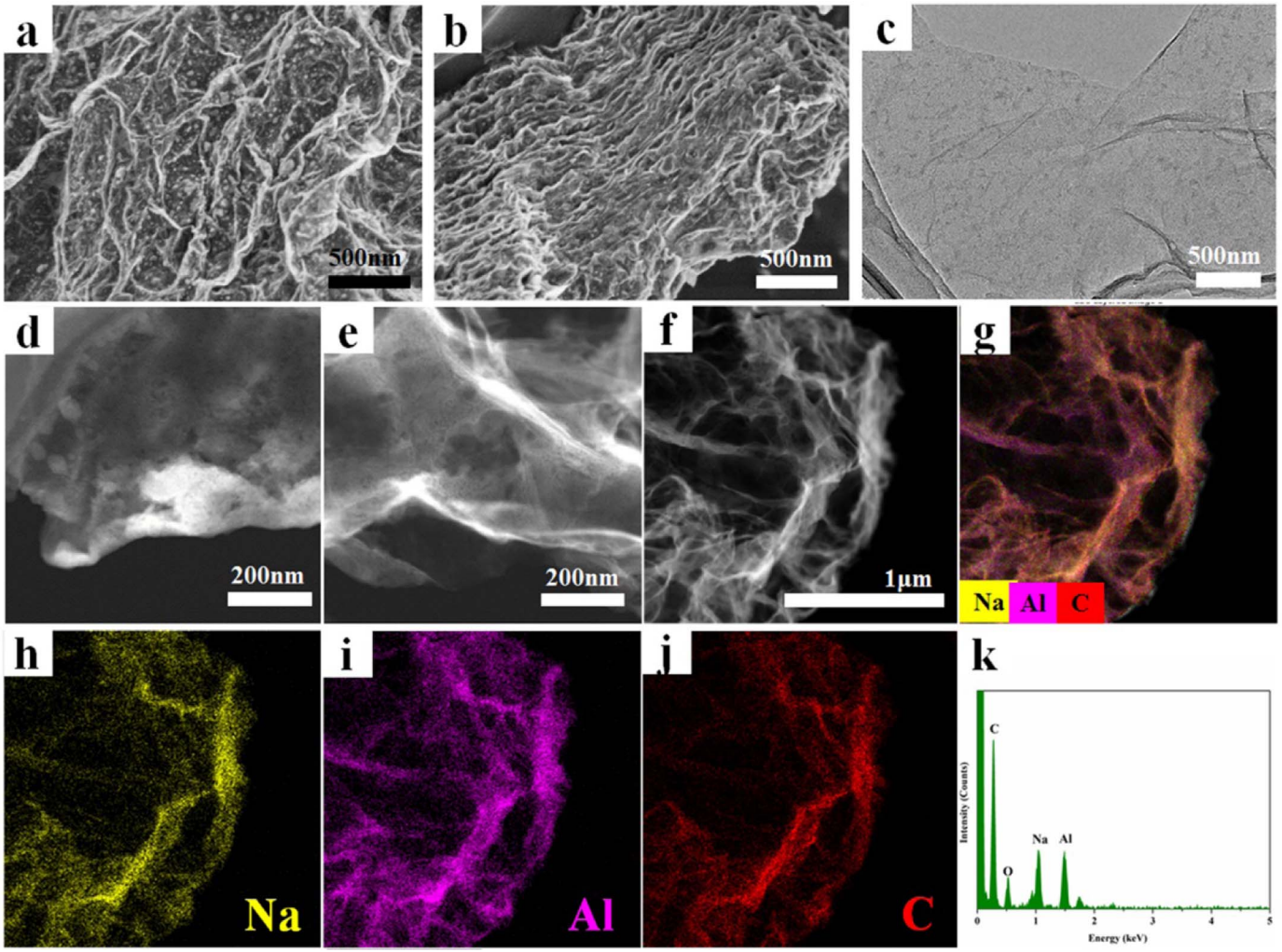

Fig. 2. FE-SEM images (a, b), TEM images (c), and STEM images (d, e, f) of SAH@G-50. Elemental mapping (g), the corresponding elemental mapping of Na (h), Al (i), and C (j), and the EDX spectrum (k) of SAH@G-50 composite.

could almost approach saturation of the hydrogen release process in only 40 min at 160 °C. This result was further proved by the XRD results (Fig. 4**d**), in which the main phases of NaH and Al were observed for SAH@G-50 after dehydrogenation at 160 °C for 40 min, with the presence of a small amount of Na_3AlH_6. In comparison, a mixture of sharp diffraction peaks of $NaAlH_4$ and weak peaks of Al was observed for the ball-milled composite even after being heated for a prolonged time of 100 min at 160 °C, which demonstrates the slight decomposition of $NaAlH_4$. Moreover, only a period of less than 20 min is required for the full dehydrogenation of SAH@G-50 with a maximum hydrogen capacity of 5.6 wt% upon heating at 180 °C. Even at a temperature as low as 120 °C, the SAH@G-50 desorbed approximately 3.8 wt% hydrogen, while only a capacity of 0.3 wt% was observed for the $NaAlH_4$/G composite, not to mention the bulk $NaAlH_4$ (Fig. S9). To quantitatively characterize the enhanced hydrogen release performance of $NaAlH_4$, the apparent activation energy (E_a) was further demonstrated based on the Johnson-Mehl-Avrami (JMA) model in Eq. (S1) and the Arrhenius equation in Eq. (S3). The E_a of the as-prepared SAH@G-50 was calculated to be approximately 68.23 kJ mol^{-1} (Fig. S10), much lower than that of bulk $NaAlH_4$ (128 kJ mol^{-1}) [15]. This directly demonstrates that, resulting from the favorable molecular interaction between graphene and $NaAlH_4$ with homogeneous and intimate contact and the significant reduction of particle size, the weakening of Al-H bonds could significantly improve the hydrogen storage properties of $NaAlH_4$.

Tremendous degradation of hydrogen capacity owing to the sintering effect and phase separation of NaH and Al is another major obstacle for the practical application of $NaAlH_4$. It could be clearly observed that, in the ball-milled composite $NaAlH_4$/G, the amount of hydrogen released was greatly decreased from 2.5 to 1.6 wt% after only three cycles (Fig. 5**a**), so that it exhibited a capacity retention of only 64% for the 3rd cycle (Fig. 5**b**). In strong contrast, there is no obvious degradation in the cycling performance of SAH@G-50, and the capacity retention remains over 98% after 20 cycles. In particular, a reversible capacity of 5.48 wt% could be achieved for SAH@G-50, even after a total of 20 cycles of hydrogenation and dehydrogenation, corresponding to a degradation rate of only 0.006 wt% $cycle^{-1}$. More importantly, the dehydrogenation kinetics for SAH@G-50 is well maintained from the first to the 20th cycle, and a complete dehydrogenation process could still be achieved at 160 °C within less than 40 min. All the diffraction peaks of the hydrogenated products of SAH@G-50 could be clearly indexed to $NaAlH_4$, without the presence of any impurity, which confirms its excellent cycling stability (Fig. 5**c**). In comparison, only weak reflections of Na_3AlH_6 and Al were observed for the rehydrogenated $NaAlH_4$/G after 3 cycles, along with the absence of $NaAlH_4$. After 20 cycles of hydrogen storage process, the homogeneous distribution of $NaAlH_4$ NPs on the graphene layers was well preserved with no obvious aggregation, as shown in the FE-SEM and STEM images (Fig. 5**d**, **e**). The corresponding EDX mapping (Fig. S11) provides further evidence of the uniform distribution of $NaAlH_4$ on graphene after 20 cycles of reversible hydrogenation/dehydrogenation process. In addition, the average particle size of $NaAlH_4$ after cycling is calculated to be

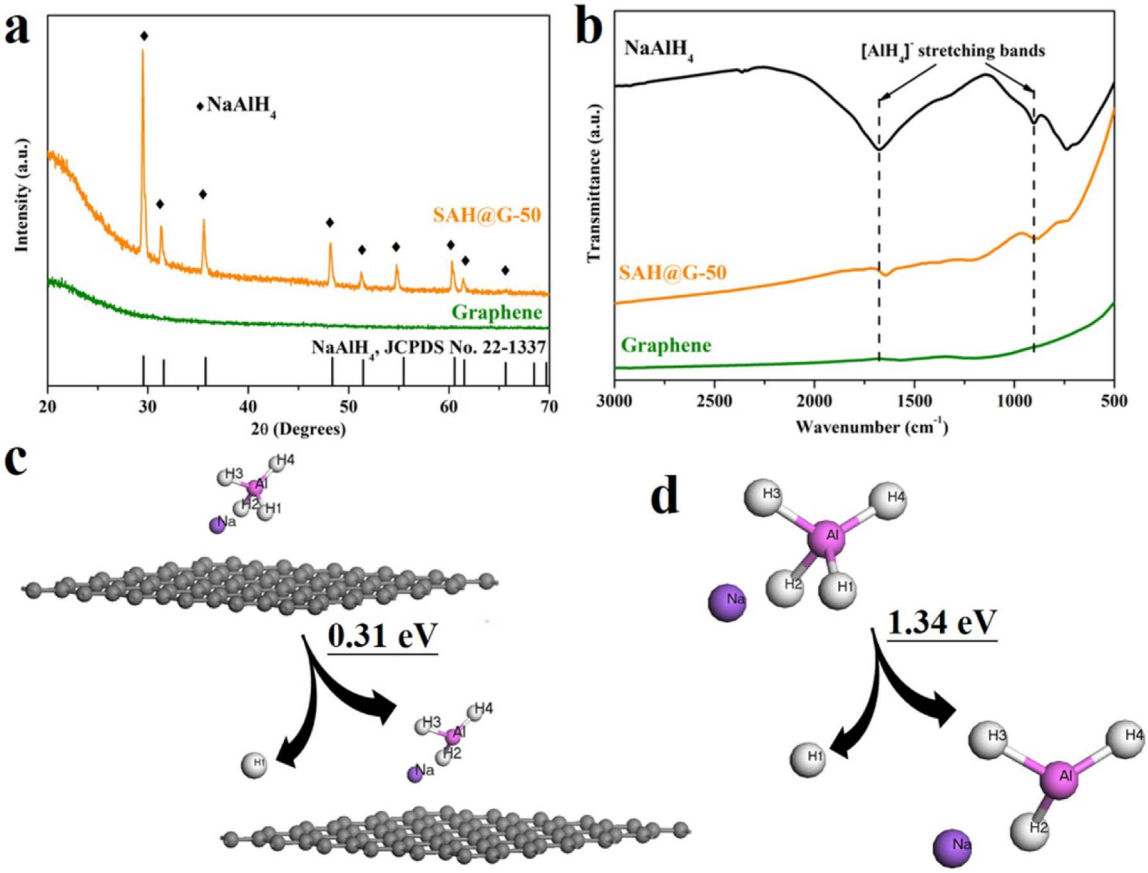

Fig. 3. (a) PXRD patterns and (b) FTIR spectra of the as-prepared SAH@G-50, in comparison with pristine $NaAlH_4$ and graphene. Energies required for the removal of hydrogen from $NaAlH_4$ with (c) and without (d) the presence of graphene.

approximately 18.9 nm (Fig. S12), which provides direct evidence of the fact that the favorable interaction and the intimate contact between graphene and $NaAlH_4$ could restrict the particle growth and aggregation to a large extent during the dehydrogenation and hydrogenation cycles, leading to the enhancement of cycling stability. In a comprehensive view, compared with other latest hydrogen storage systems (Table S1), the SAH@G-50 exhibits superior reversible hydrogen storage performance in terms of reversible temperature and cycling stability via a simple reversible method of direct hydrogenation and dehydrogenation.

To evaluate the electrochemical lithium storage performance of SAH@G-50 electrode, cyclic voltammetry (CV), and galvanostatic charge-discharge cycling were conducted using CR2032 coin cells with lithium foil as counter/reference electrode. In the first cycle, the cathodic scan is dominated by the formation of the solid-electrolyte interphase (SEI), starting at approximately 0.69 V and followed with a sharp signal at a low potential (< 0.25 V vs. Li), which is attributed to the lithiation of Al resulting from the reduction of $NaAlH_4$ (Fig. 6**a**). In the initial charge process, two peaks at 0.5 V and 0.8 V are observed, which could be ascribed to the reversible delithiation of Al and the reformation of $LiNa_2AlH_6$, respectively. This is in good agreement with previous reports [33]. It validates that the electrochemical reaction of SAH@G-50 for cycling lithium storage should be based on Eqs. (3) and (4). In the subsequent cycles, the CV curves of SAH@G-50 are almost overlapping, demonstrating its good reversibility. By comparison, bulk $NaAlH_4$ acts differently within the same potential range, and only the peak at 0.5 V versus Li exists in the first anodic cycle, suggesting poor reversibility of these reactions (Fig. 6**b**). Fig. 6**c** presents the cycling performance of SAH@G-50 at a current density of 100 mA g^{-1}, with bulk $NaAlH_4$ and pure graphene (Fig. S13) included for comparison. It should be noted that all the specific capacity is based on the mass of $NaAlH_4$ in the composite. The SAH@G-50 electrode exhibits an initial discharge and charge capacity of 1995 and 1710 mA h g^{-1}, respectively corresponding to a coulombic efficiency (CE) of 85.7%. The capacity loss can be mainly ascribed to the formation of SEI films on the electrode surface or the irreversible side reactions with electrolyte, in accordance with the CV curves. The specific discharge capacity slowly decayed and then was stabilized at ~698 mAh g^{-1} after 200 cycles. In strong contrast, although bulk $NaAlH_4$ electrode displayed an initial discharge capacity of 2057 mA h g^{-1}, the capacity rapidly decreased to less than 100 mAh g^{-1} after only 20 cycles, which is consistent with the results reported previously [16]. The rate capability test of SAH@G-50 electrode at current densities ranging from 50 to 500 mA g^{-1} demonstrates that this electrode could deliver average capacities of 1495, 1273, 924, 620, and 529 mAh g^{-1} at 50, 100, 200, 300, and 500 mA g^{-1}, respectively (Fig. 6**d**). When switching back to 100 mA g^{-1} after the high-rate cycling, the capacity can return to 950 mA h g^{-1}. In comparison, the capacity of bulk $NaAlH_4$ electrode rapidly decreased to only 100 mAh g^{-1} at 500 mA g^{-1}. This validates the strong tolerance of SAH@G-50 electrode toward rapid lithium ion insertion and extraction. Furthermore, the SAH@G-50 electrode delivered an impressive discharge capacity of 522 mAh g^{-1} after 200 cycles at a high current density of 500 mA g^{-1}, with a high CE of around 100% through the whole cycling process, which further demonstrates its superior reversibility.

To investigate the superior electrochemical properties of SAH@G-50 electrode, electrochemical impedance spectroscopy (EIS) was carried out. As shown in Fig. S14, each of the Nyquist plots contains a depressed semicircle at medium and high frequencies, corresponding to the charge-transfer impedance at the interface between the electrolyte and the working electrode, followed by a straight line with constant inclining angle at low frequencies. It could be readily observed that the

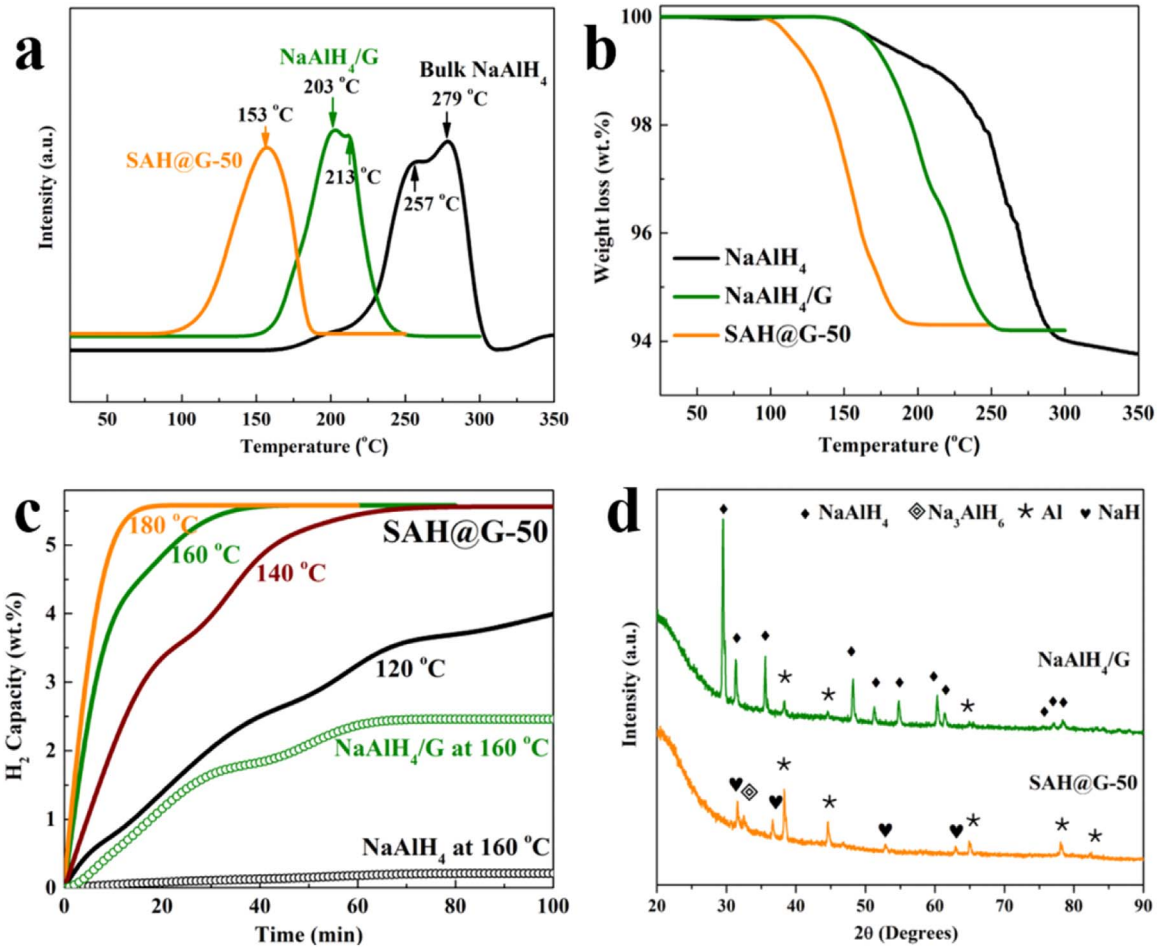

Fig. 4. Mass spectra (a) and thermogravimetric analysis curves (b) of the as-prepared SAH@G-50 compared with bulk $NaAlH_4$ and the ball-milled composite of $NaAlH_4$ and graphene ($NaAlH_4$/G). (c) Isothermal dehydrogenation of SAH@G-50 in comparison with $NaAlH_4$ and the ball-milled $NaAlH_4$/G composite at various temperatures. (d) XRD patterns of SAH@G-50 after dehydrogenation for 40 min and the ball-milled $NaAlH_4$/G composite after dehydrogenation for 100 min at 160 °C.

SAH@G-50 electrode displays a much smaller diameter of the semicircle as compared with $NaAlH_4$ electrode, indicating that SAH@G-50 has higher electrical conductivity and faster kinetics. The poor reversible capacity of $NaAlH_4$ is mainly due to the low conductivity, huge volume changes, and severe aggregation during the cycling process. In SAH@G-50, the presence of graphene with uniform distribution and favorable interaction with $NaAlH_4$ could significantly improve the conductivity of the composite, buffer the big volume change, and prevent the growth and aggregation of nanosized particles during the lithiation and delithiation process. TEM observations validate that SAH@G-50 maintains its original structure, with the $NaAlH_4$ NPs in SAH@G-50 still uniformly anchored on the graphene layers after 100 cycles (Fig. S15). The selected area diffraction patterns (SADP) (inset of Fig. S15) demonstrates the amorphous nature of SAH@G-50 after cycling, which is in good agreement with XRD results (Fig. S16). This phenomenon is mainly attributed to the formation of thick SEI films and the smaller particle size due to the pulverization of $NaAlH_4$ NPs during the cycling charge and discharge process. Thereby, in comparison with the pristine $NaAlH_4$, the SAH@G-50 electrode exhibits a higher capacity and better cycling performance by taking advantage of the synergistic effects of the molecular interaction between graphene and $NaAlH_4$ and the significant decrease in the particle size.

3. Conclusion

In summary, we have developed a facile SEID method to realize the homogeneous distribution of $NaAlH_4$ NPs on graphene with intimate contact. This unique nanostructure contributes to the effective hydrogen and lithium storage in $NaAlH_4$, among which, graphene could not only act as a structural support for the formation of uniformly dispersed $NaAlH_4$, but also improve thermal (electron) transport of the system and restrict $NaAlH_4$ NPs from growing and aggregating to a large extent during cycling, leading to the enhancement of cycling stability. Moreover, the favorable interaction between graphene and $NaAlH_4$ could effectively tailor the strength of Al–H bonds of $NaAlH_4$ and therefore promote their breaking and recombination towards advanced hydrogen (lithium) storage performance. Additionally, the significant reduction of particle size of $NaAlH_4$ down to only ~12 nm is also favorable for improving the kinetics for hydrogen (lithium) storage through the reduced diffusion pathway and more active reaction sites on the surface. It is these synergistic effects that significantly enhance the hydrogen and lithium storage performance of $NaAlH_4$. Moreover, this strategy represents a highly novel approach based on tailoring the molecular bonds of metal hydrides with advantageous structures to promote their energy storage performance.

4. Experimental details

4.1. Fabrication of $NaAlH_4$@graphene nanostructures

All chemicals were purchased from Sigma-Aldrich and used as received without further purification. Graphene (specific surface area: 700–1000 $m^2\ g^{-1}$, electrical conductivity: 700–1500 $S\ m^{-1}$) was purchased from Simbatt Energy Technology Co. Ltd. The $NaAlH_4$ NPs grown on graphene with various mass loadings were fabricated via a facile SEID method (Fig. 1**a**). Firstly, 1 mol $NaAlH_4$ was dissolved into

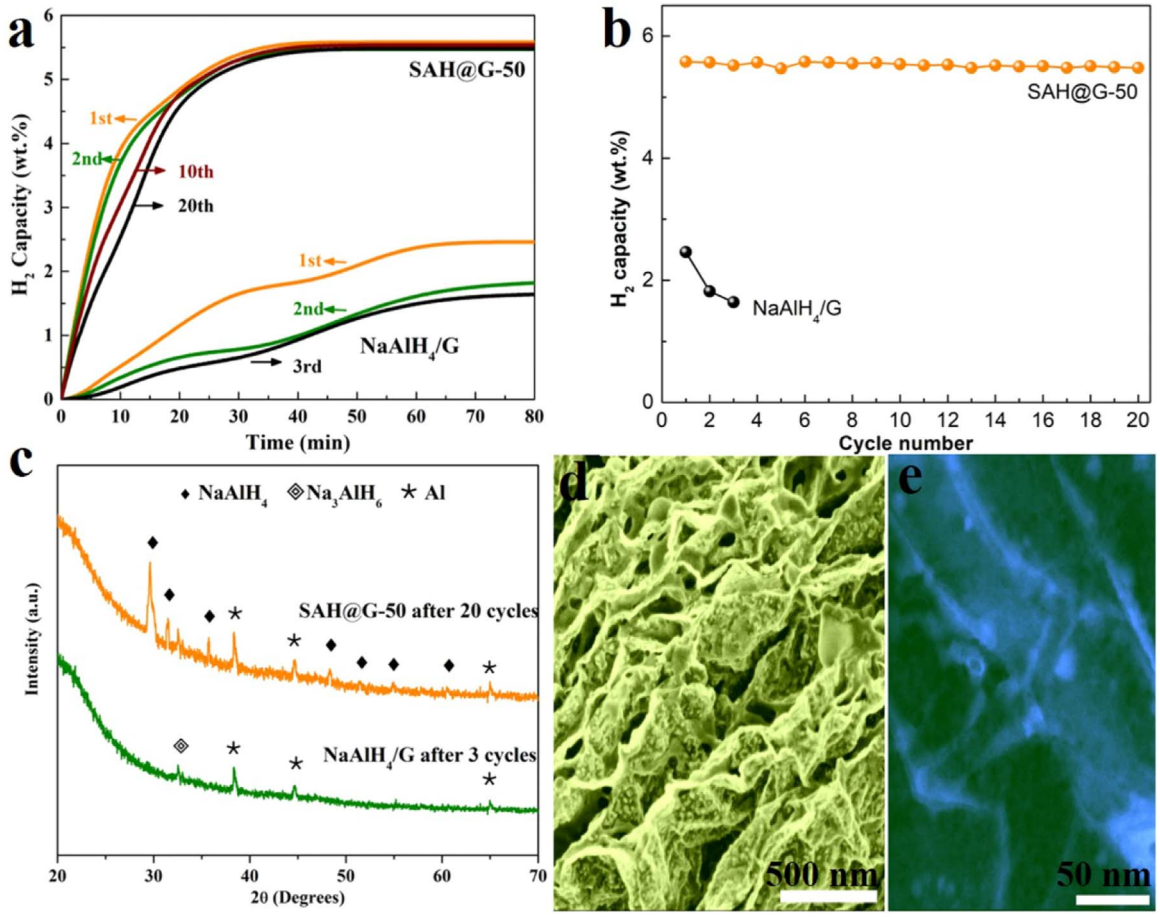

Fig. 5. (a) Reversible dehydrogenation of SAH@G-50 in comparison with the ball-milled $NaAlH_4$/G composite at 160 °C. (b) Cycling capacity of the as-prepared SAH@G-50 compared with the ball-milled $NaAlH_4$/G composite. (c) XRD patterns of SAH@G-50 after 20 cycles of hydrogenation and of the ball-milled $NaAlH_4$/G composite after 3 cycles of hydrogenation at 160 °C. (d) FE-SEM and (e) STEM images of SAH@G-50 after 20 cycles of hydrogen storage.

6 mL tetrahydrofuran (THF) under ultrasonic stirring for 20 min. Secondly, 2 mL $NaAlH_4$ in the THF solution and graphene were mixed in a pressure reactor vessel and kept under ultrasonic dispersion for 1 h. A certain amount of graphene (0.156 g, 0.039 g, and 0.015 g) was added to synthesize SAH@G hybrids with different loadings of $NaAlH_4$ (SAH@G-10, SAH@G-30, and SAH@G-50). All the above synthesis procedures were carried out in a argon-filled glove box (Mikrouna Universal) with moisture and oxygen contents below 0.1 ppm. The solvent infiltration of $NaAlH_4$ was then carried out at 120 °C under a hydrogen pressure of 50 atm for 10 h. Finally, the products were dried at room temperature via dynamic vacuum on a Schlenk line, leading to the formation of SAH@G hybrid.

4.2. Materials characterizations

The crystalline structures of samples were characterized by powder X-ray diffraction (XRD; D8 Advance, Bruker AXS) with Cu Kα radiation. To prevent any possible reactions between samples and air during the XRD measurements, amorphous tape was used to cover the samples. FTIR spectra were recorded on a Genesis II spectrophotometer (Mattson). The FTIR spectra was obtained over 32 scans in absorption mode at a resolution of 4 cm^{-1}. Thermogravimetric analysis (TG; Netzsch STA449 F3) in conjunction with mass spectrometry (MS; Hiden HPR 20) was performed under Ar flow at a ramp rate of 5 °C min^{-1}. The morphology and composition of samples were determined using an FE-SEM (JEOL 7500FA, Tokyo, Japan) and a TEM (JEOL 2011 F, Tokyo, Japan) coupled with an EDX spectrometer. Samples for TEM and SEM tests were first dispersed on Cu grids and conducting resin in the glove box, respectively, and then rapidly transferred into the chambers for testing within a few seconds. The isothermal dehydrogenation properties were measured via a volumetric method based on Sieverts' law using a Sieverts' device, denoted as a gas reaction controller (GRC, Advanced Materials Corp., USA). The apparatus was carefully calibrated by adopting $LaNi_5$ as a reference sample with an accuracy of ± 1%. The hydrogen absorption measurements were conducted at 160 °C under an initial hydrogen pressure of 80 atm, and the hydrogen desorption properties were calculated under a hydrogen pressure below 0.01 atm.

4.3. Electrochemical measurements

Electrochemical experiments were carried out within 2032 coin-type half-battery cells assembled with a pure lithium foil as counter electrode, and Whatman borosilicate glass-fiber filter paper as separator. The electrolyte consisted of 1 M $LiPF_6$ in ethylene carbonate (EC) / dimethyl carbonate (DMC) / diethyl carbonate (DEC) (1:1:1, volume ratio) solution. The working electrodes were fabricated by grinding the active materials samples, acetylene black, and binder at a weight ratio of 8:1:1, coating the product on nickel foam, and drying it in vacuum at 60 °C for 24 h. Poly(methyl methacrylate) (PMMA) binder was dissolved in DMC. The cells were assembled in an argon-filled glove box with concentrations of moisture and oxygen kept below 0.1 ppm. CV and EIS were both performed using a CHI660D electrochemistry workstation at room temperature. CV curves were collected at a scan rate of 0.1 mV s^{-1} in the potential range of 0.01–3.0 V (vs. Li^+/Li), and EIS was carried out from 100 kHz to 0.01 Hz. The cycling performance and rate stability of cells were tested using a Land Battery Test System between 0.001 V and 3.0 V (vs. Li^+ /Li) at different constant current densities.

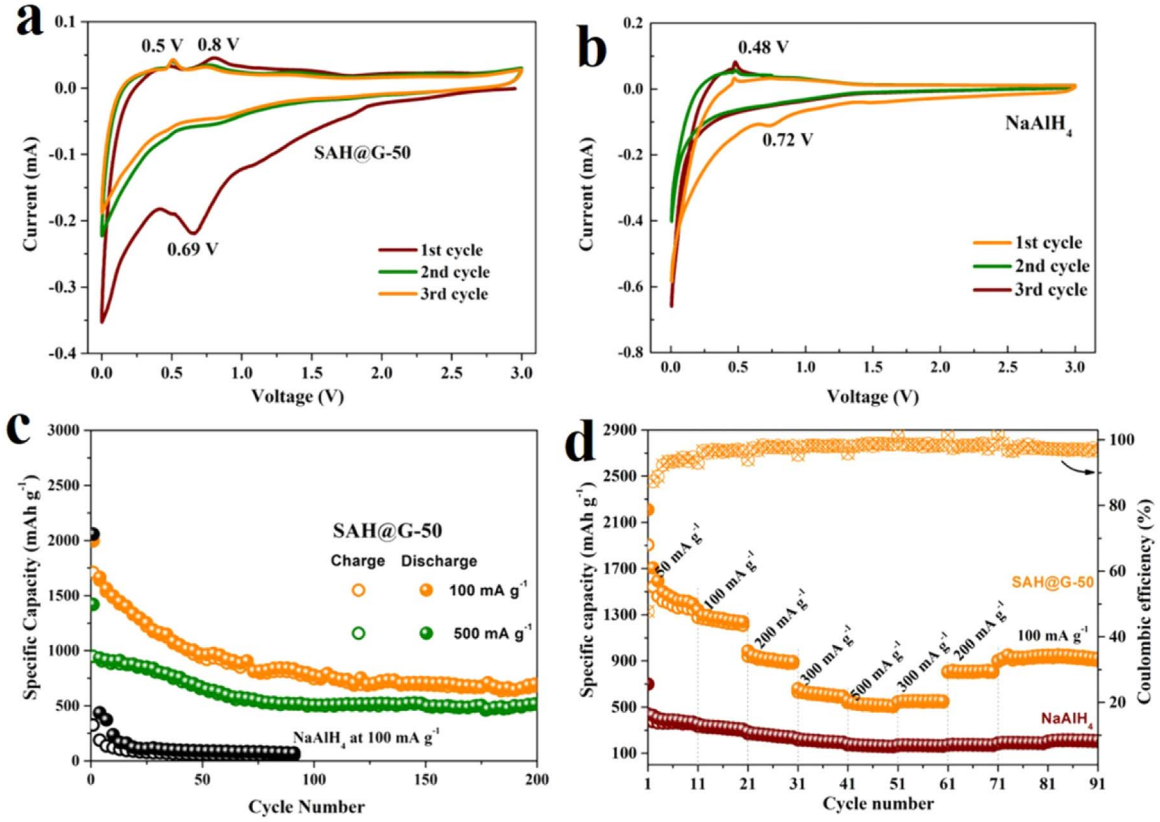

Fig. 6. Representative CV curves for the first 3 cycles of the SAH@G-50 (a) and bulk $NaAlH_4$ (b) electrodes at a scan rate of 0.1 mV s^{-1}. (c) Comparison of the specific capacities of SAH@G-50 with bulk $NaAlH_4$ at the current densities of 100 mA g^{-1} and 500 mA g^{-1}. (d) Rate performance of SAH@G-50 electrode, with bulk $NaAlH_4$ electrode included for comparison.

Acknowledgements

This work was partially supported by the National Science Fund for Distinguished Young Scholars (51625102), National Key Research and Development Program of China (2017YFA0204600), the National Natural Science Foundation of China (51471053), the Science and Technology Commission of Shanghai Municipality (17XD1400700), and a Discovery Early Career Researcher Award (DE170100362). The authors also would like to thank Prof. Dianwu Zhou in Hunan University for the support of the DFT calculations software, and Dr. Tania Silver for critical reading of the manuscript.

NotesDeclarations of interest

None.

Appendix A. Supporting information

Supplementary data associated with this article can be found in the online version at doi:10.1016/j.ensm.2018.07.020.

References

[1] R. Raccichini, A. Varzi, S. Passerini, B. Scrosati, Nat. Mater. 14 (2014) 271–279.
[2] Q.-L. Zhu, Q. Xu, Energy Environ. Sci. 8 (2015) 478–512.
[3] L. Ouyang, W. Chen, J. Liu, M. Felderhoff, H. Wang, M. Zhu, Adv. Energy Mater. 7 (2017) 1700299.
[4] L.Z. Ouyang, X.S. Yang, M. Zhu, J.W. Liu, H.W. Dong, D.L. Sun, J. Zou, X.D. Yao, J. Phys. Chem. C. 118 (2014) 7808–7820.
[5] R. Mohtadi, S.-i Orimo, Nat. Rev. Mater. 2 (2016) 16091.
[6] Y. Sun, N. Liu, Y. Cui, Nat. Energy 1 (2016) 16071.
[7] J. Zhang, S. Yan, H. Qu, Int. J. Hydrog. Energy 43 (2018) 1545–1565.
[8] Y. Pang, Y. Liu, M. Gao, L. Ouyang, J. Liu, H. Wang, M. Zhu, H. Pan, Nat. Commun. 5 (2014) 3519.
[9] M. Paskevicius, L.H. Jepsen, P. Schouwink, R. Cerny, D.B. Ravnsbaek, Y. Filinchuk, M. Dornheim, F. Besenbacher, Chem. Soc. Rev. 46 (2017) 1565–1634.
[10] X. Zhang, Y. Liu, K. Wang, Y. Li, M. Gao, H. Pan, ChemSusChem 8 (2015) 4180–4188.
[11] S. Deng, V. Tjoa, H.M. Fan, H.R. Tan, D.C. Sayle, M. Olivo, S. Mhaisalkar, J. Wei, C.H. Sow, J. Am. Chem. Soc. 134 (2012) 4905–4917.
[12] T. Mueller, G. Ceder, ACS Nano 4 (2010) 5647–5656.
[13] X. Zhang, Y. Liu, Y. Pang, M. Gao, H. Pan, J. Mater. Chem. A 2 (2014) 1847–1854.
[14] Y. Li, F. Fang, H. Fu, J. Qiu, Y. Song, Y. Li, D. Sun, Q. Zhang, L. Ouyang, M. Zhu, J. Mater. Chem. A 1 (2013) 5238–5246.
[15] X. Fan, X. Xiao, J. Shao, L. Zhang, S. Li, H. Ge, Q. Wang, L. Chen, Nano Energy 2 (2013) 995–1003.
[16] J.A. Teprovich, J. Zhang, H. Colón-Mercado, F. Cuevas, B. Peters, S. Greenway, R. Zidan, M. Latroche, J. Phys. Chem. C 119 (2015) 4666–4674.
[17] F. Wu, Z. Chen, B. Lei, J. Wang, K. Xie, Y. Song, D. Sun, F. Fang, Electrochim. Acta 257 (2017) 321–327.
[18] L. Silvestri, A. Paolone, L. Cirrincione, P. Stallworth, S. Greenbaum, S. Panero, S. Brutti, P. Reale, J. Electrochem. Soc. 164 (2017) A1120–A1125.
[19] L. Silvestri, M.A. Navarra, S. Brutti, P. Reale, Electrochim. Acta 253 (2017) 218–226.
[20] P. Huen, F. Peru, G. Charalambopoulou, T.A. Steriotis, T.R. Jensen, D.B. Ravnsbæk, ACS Omega 2 (2017) 1956–1967.
[21] W.-B. Li, L. Li, Q.-L. Ren, Y.-J. Wang, L.-F. Jiao, H.-T. Yuan, Rare Met. 34 (2015) 679–682.
[22] L. Li, F. Qiu, Y. Wang, Y. Wang, G. Liu, C. Yan, C. An, Y. Xu, D. Song, L. Jiao, H. Yuan, J. Mater. Chem. 22 (2012) 3127–3132.
[23] V. Stavila, R.K. Bhakta, T.M. Alam, E.H. Majzoub, M.D. Allendorf, ACS Nano 6 (2012) 9807–9817.
[24] Y. Li, G. Zhou, F. Fang, X. Yu, Q. Zhang, L. Ouyang, M. Zhu, D. Sun, Acta Mater. 59 (2011) 1829–1838.
[25] A.J. Du, S.C. Smith, G.Q. Lu, Phys. Rev. B 74 (2006) 193405.
[26] L. Xu, Q. Ge, Int. J. Hydrog. Energy 38 (2013) 3670–3680.
[27] Q. Li, P. Xu, W. Gao, S. Ma, G. Zhang, R. Cao, J. Cho, H.-L. Wang, G. Wu, Adv. Mater. 26 (2014) 1378–1386.
[28] L. Ouyang, Z. Cao, H. Wang, R. Hu, M. Zhu, J. Alloy. Compd. 691 (2017) 422–435.
[29] L. Ouyang, L. Guo, W. Cai, J. Ye, R. Hu, J. Liu, L. Yang, M. Zhu, J. Mater. Chem. A 2 (2014) 11280–11285.
[30] L. Ouyang, Z. Cao, L. Li, H. Wang, J. Liu, D. Min, Y. Chen, F. Xiao, R. Tang, M. Zhu, Int. J. Hydrog. Energy 39 (2014) 12765–12772.
[31] R. Wu, H. Du, Z. Wang, M. Gao, H. Pan, Y. Liu, J. Power Sources 327 (2016) 519–525.
[32] Q. Gao, G. Xia, X. Yu, Nanoscale 9 (2017) 14612–14619.
[33] W. Zeng, S.W. Buckner, P.A. Jelliss, ACS Omega 2 (2017) 2034–2040.